energies

MDPI

Article

ZnCu Metal–Organic Framework Electrocatalysts for Efficient Ammonia Decomposition to Hydrogen

Mingguang Ouyang, Geng Chen, Weitao Ning, Xiaoyang Wang *, Xiaojiang Mu and Lei Miao *

Guangxi Novel Battery Materials Research Center of Engineering Technology, State Key Laboratory of Featured Metal Materials and Life-Cycle Safety for Composite Structures, School of Physical Science and Technology, Guangxi University, Nanning 530004, China; 2207301105@st.gxu.edu.cn (M.O.); 11610834@mail.sustech.edu.cn (G.C.); 2312270302@st.gxu.edu.cn (W.N.); xjmu@gxu.edu.cn (X.M.)

* Correspondence: wangxy@gxu.edu.cn (X.W.); miaolei@gxu.edu.cn (L.M.)

Abstract

The electrocatalytic decomposition of ammonia represents a promising route for sustainable hydrogen production, yet current systems rely heavily on noble metal catalysts with prohibitive costs and limited durability. A critical challenge lies in developing non-noble electrocatalysts that simultaneously achieve high active site exposure, optimized electronic configurations, and robust structural stability. Addressing these requirements, this study strategically engineered Cu-doped ZIF-8 architectures via in situ growth on nickel foam (NF) substrates through a facile room-temperature hydrothermal synthesis approach. Systematic optimization of the Cu/Zn molar ratio revealed that $Cu_{0.7}Zn_{0.3}$-ZIF/NF achieved optimal performance, exhibiting a distinctive nanoflower-like architecture that substantially increased accessible active sites. The hybrid catalyst demonstrated superior electrocatalytic performance with a current density of 124 mA cm^{-2} at 1.6 V vs. RHE and a notably low Tafel slope of 30.94 mV dec^{-1}, outperforming both Zn-ZIF/NF (39.45 mV dec^{-1}) and Cu-ZIF/NF (31.39 mV dec^{-1}). Combined XPS and EDS analyses unveiled a synergistic electronic structure modulation between Zn and Cu, which facilitated charge transfer and enhanced catalytic efficiency. A gas chromatography product analysis identified H_2 and N_2 as the primary gaseous products, confirming the predominant occurrence of the ammonia oxidation reaction (AOR). This study not only presents a noble metal-free electrocatalyst with exceptional efficiency and durability for ammonia decomposition but also demonstrates the significant potential of MOF-derived materials in sustainable hydrogen production technologies.

Keywords: AOR; ZIF-8; non-noble metal catalyst; copper doping; hydrogen production

check for updates

Academic Editor: George Avgouropoulos

Received: 13 June 2025
Revised: 11 July 2025
Accepted: 16 July 2025
Published: 21 July 2025

Citation: Ouyang, M.; Chen, G.; Ning, W.; Wang, X.; Mu, X.; Miao, L. ZnCu Metal–Organic Framework Electrocatalysts for Efficient Ammonia Decomposition to Hydrogen. *Energies* **2025**, *18*, 3871. https://doi.org/10.3390/en18143871

Copyright: © 2025 by the authors. Licensee MDPI, Basel, Switzerland. This article is an open access article distributed under the terms and conditions of the Creative Commons Attribution (CC BY) license (https://creativecommons.org/licenses/by/4.0/).

1. Introduction

In recent years, as energy policy has shifted towards greener/sustainable technologies, hydrogen has emerged as a desirable energy source [1,2]. However, due to the inherent limitations of hydrogen with regard to storage and transportation, an increasing number of researchers are seeking a high-density hydrogen storage medium [3]. Ammonia exhibits a mass hydrogen storage density of up to 17.6 wt%, which is significantly higher than that of traditional materials such as methanol and water. Moreover, ammonia can be produced in substantial quantities through the Haber–Bosch process and transported using existing storage and transportation methods, thereby providing a substantial supply of low-cost hydrogen storage materials [4]. In addition, the electrocatalytic ammonia oxidation reaction (AOR) for hydrogen production offers a green and efficient alternative [5], featuring

a theoretical voltage of 0.06 V, significantly lower than conventional water electrolysis (1.23 V) [6–8]. Additionally, this technology demonstrates important applications in ammonia fuel cells [7–10] and ammonia–nitrogen wastewater treatment [11,12]. Consequently, electrolytic ammonia hydrogen production represents a highly promising pathway for hydrogen generation.

However, the electrolytic AOR is a six-electron proton-coupled process with a high kinetic barrier that severely limits electrolysis efficiency. This results in slow reaction kinetics and increased energy requirements to overcome the reaction barrier [13], thereby restricting ammonia decomposition application. Consequently, developing low overpotential electrocatalysts for ammonia decomposition anode catalysts is imperative. Currently, AOR catalysts are categorized as either noble metal catalysts [14–16] or non-noble metal catalysts [17,18]. While noble metal catalysts reduce the reaction barriers effectively, most suffer from poor stability due to strong N* that causes rapid catalyst deactivation [3,4,19]. Meanwhile, considering that the raw materials of noble metal catalysts are too expensive, researchers started to search for cheap catalysts for efficient AOR. As a result, more and more research has focused on non-noble metal catalysts, and the current studies on non-noble metal catalysts are mainly focused on transition metal alloys [20], transition metal oxides [21], transition metal phosphorus/sulfides [22,23], and other types of catalysts. Compared with noble metal catalysts, the stability of non-noble metal catalysts has been substantially improved, Nevertheless, they exhibit substantially higher overpotentials than noble metal catalysts. Key challenges involve high kinetic barriers and catalyst stability issues. Noble metal catalysts undergo rapid deactivation owing to strong N* adsorption, while non-noble metal catalysts (e.g., transition metal alloys/oxides) exhibit limited activity.

Metal–organic frameworks (MOFs) feature high specific surface areas and tunability, enabling applications in energy, gas adsorption/desorption, and catalysis [24–26]. Although their high specific surface areas and abundant unsaturated metal sites provide numerous catalytic active sites, most MOFs exhibit poor conductivity due to insufficient charge carriers and transport pathways. Additionally, limited aqueous stability constrains their practical use in electrocatalysis [27–33]. In contrast to most MOFs, zeolitic imidazolate framework-8 (ZIF-8) demonstrates excellent water stability and low cost. We therefore selected ZIF-8 to explore the MOF potential in electrocatalytic ammonia decomposition. To enhance conductivity and active site utilization, ZIF-8 was synthesized in situ on nickel foam (NF) [34,35]. Given the established electrocatalytic performance of Cu-based catalysts in AOR [36–40], we introduced copper doping to provide additional active sites for improved AOR activity [41,42].

In this study, Cu_xZn_{1-x}-ZIF/NF anodic catalysts were synthesized via a simple room-temperature aqueous synthesis method for AOR application. The materials were systematically characterized by scanning electron microscopy (SEM) and X-ray photoelectron spectroscopy (XPS) to analyze their crystal structures and chemical states. The SEM results demonstrated that the microstructures of $Cu_{0.7}Zn_{0.3}$-ZIF/NF with the unusual "nanoflower" structure exposed a greater number of active sites, thereby facilitating the catalytic reaction. The SEM results demonstrated that the microstructure of $Cu_{0.7}Zn_{0.3}$-ZIF/NF, featuring the distinctive "nanoflower" configuration, exhibited an increased number of active sites and thereby promoted the catalytic reaction. Moreover, electrochemical tests demonstrated that the $Cu_{0.7}Zn_{0.3}$-ZIF/NF catalyst exhibited a current density of up to 124 mA/cm^2 (1.6 V vs. RHE). Subsequent chronoamperometry (i-t) tests further corroborated the remarkable stability of the catalyst. In this paper, Cu-doped ZIF-8/NF catalysts were synthesized by a simple room-temperature hydrothermal method. These catalysts have efficient electrocatalytic AOR performance and provide a new strategy for the application of MOF in electrocatalysis.

2. Materials and Methods

2.1. Synthesis of Cu_xZn_{1-x}-ZIF/NF Catalysts

Preparation method: all reagents were directly used without further refinement. Cu_xZn_{1-x}-ZIF/NF catalysts were synthesized via a room-temperature aqueous synthesis method, as shown in Figure 1. Briefly, 1.08 g of 2-methylimidazole (98%, Aladdin, Wallingford, CT, USA) and 0.66 g (2.2 mmol) of zinc nitrate hexahydrate (99%, Sinopharm Chemical Reagent Co., Ltd., Shanghai, China) were dissolved and mixed separately and then added to NF with full stirring for 3 h to make ZIF-8 grow uniformly on the NF surface. Finally, this mixture was dried in a 60 °C vacuum. The Zn-ZIF/NF catalyst was obtained by drying in a drying oven for 6 h; the molar ratio of the fixed metal source to 2-methylimidazole was kept constant. For Cu doping using copper nitrate trihydrate compounds (97%, Aladdin), the molarities of Cu and Zn sources were fixed at 2.2 mmol, and the catalysts were prepared by weighing x of the Cu source molarities/metal molarities and were denoted as Cu_xZn_{1-x}-ZIF/NF, respectively.

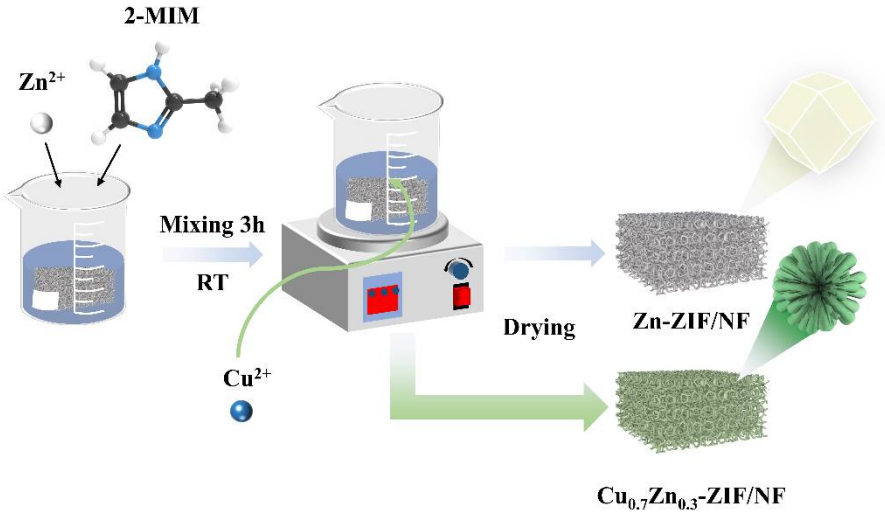


Figure 1. Cu_xZn_{1-x}-ZIF/NF catalyst preparation flow.

2.2. Material Characterization

The surface morphology and microstructure of the catalysts were analyzed using a ZEISS Gemini 300 SEM (Zeiss, Oberkochen, Germany) at a 5 kV working voltage. X-ray energy-dispersive spectroscopy (EDS) mapping was performed at an acceleration voltage of 15 kV to acquire elemental composition. The phase structure of the catalyst was characterized using an A24A10 X-ray powder diffractometer from BRUKER AXS GMBH in Karlsruhe, Germany. Cu-Kα (λ = 1.54056 Å) was used as the X-ray radiation source, and all operating parameters were set to 40 kV and 40 mA. In the actual test, a scanning rate of 8°/min was selected for scanning in the range of 3–50°. The acquisition of transmission electron microscopy (TEM) data was performed using a JEOL JEM-2100plus from Akishima, Japan. X-ray photoelectron spectroscopy (XPS) signals were recorded using a monochromatic Al Kα X-ray source (1486.6 eV) and Thermo Scientific K-Alpha XPS (Waltham, MA, USA). The binding energy of C 1 s at 284.8 eV was utilized as a calibration standard.

2.3. Electrochemical Testing

All the electrochemical measurements of the AOR were carried out at room temperature using a CHI660E electrochemical workstation (CH Instruments, Shanghai, China), a three-electrode system consisting of a graphite rod as the counter electrode, a Hg/HgO electrode (filled with 1 mol/L KOH solution) as the reference electrode, and a pre-

pared catalyst as the working electrode. The electrochemical tests were carried out in 1 M KOH + 1 M $NH_3 \cdot H_2O$ electrolyte. The AOR performance was tested by recording linear sweep voltammetry (LSV) at a scan rate of 10 mV/s in the range of −0.4 V to 0.8 V vs. Hg/HgO. The OER performance of the catalysts was confirmed by the LSV recorded at the same scan rate in 1 M KOH electrolyte. Electrochemical impedance spectroscopy (EIS) was performed in the frequency range of 0.01–100,000 Hz to measure the resistance of the catalysts at the 1 M KOH working electrode for the prepared catalysts. All catalysts were activated in 1 M KOH electrolyte, and the activation process was confirmed by cyclic voltammetry (CV) curves. The measured potentials were converted to RHE by the following equation:

$$E\ (\text{vs. RHE}) = E\ (\text{vs. Hg/HgO}) + E_{(\text{Hg/HgO})}\ (\text{vs. NHE}) + 0.059 \times \text{pH} \quad (1)$$

Chrono-current measurements usually involve the application of a constant voltage to the working electrode in order to check the change in its current. In this study, the electrode was tested for AOR stability at 0.6 V vs. Hg/HgO. Double-layer capacitance (C_{dl}) was determined by performing a CV scan of the catalyst in the range of 10–120 mV/s at a potential range without the Faraday process. This test was performed to obtain the electrochemically active surface area (ECSA) of the catalyst. Finally, the gases produced by the electrochemical reaction were directly analyzed by an online gas chromatograph (GC).

3. Results

3.1. Physical Characterization

In situ grown CuZn-ZIF/NF catalysts were synthesized on NF by a simple room-temperature hydrothermal method. In order to reveal the effect of different levels of Cu doping on the morphology of the catalysts, the catalyst materials were observed using a scanning electron microscope (SEM). As shown in Figure 2a of the microscopic morphology of the Zn-ZIF/NF catalyst, a clear dodecahedral crystal structure with sharp edges attached to the NF surface can be clearly seen. This indicates the successful preparation of the Zn-ZIF/NF catalyst. When Cu doping was up to 30%, it exhibited a structure similar to that of the original Zn-ZIF/NF, indicating that Cu doping had some influence on the morphology of the catalyst. As Cu is further doped to 50%, it appears to have a completely different microstructure from that of the parent, showing a peculiar nanoflower structure, which further verifies the effect of Cu doping on the catalyst's microscopic morphology. Meanwhile, the XRD pattern (Figure S1) reveals distinct changes, and its entirely different peak structure from Zn-ZIF/NF is primarily attributed to the coordination of Cu with 2-methylimidazole ligands [43]. This evidence suggests that the morphological changes may be related to the coordination of Cu and dimethylimidazole. When Cu was doped to 70%, it still showed the nanoflower structure, and this special structure of branching and hollowing provided a high porosity for the catalyst, which in turn promoted the transport of reactants and gaseous products, and more active sites would be exposed on its surface, contributing to the continuation of the catalytic reaction [42]. However, the internal architecture in these nanodendrites was not observed under TEM (Figure S2), which is similar to the structure of most MOF materials [43,44]. With the further increase in Cu doping, the catalyst material further grows from the original nanoflower structure to a nanosphere when the metal in the catalyst material is completely replaced by Cu (Figure 2e). At this point, only Cu is coordinated with 2-methylimidazole. However, when Cu and Zn coexist, the morphological changes observed result from the combined effects of Cu coordination with 2-methylimidazole and Zn-Cu electron transfer. To further elucidate the Zn-Cu electron transfer, we performed a detailed electronic structure analysis, as shown

in Figure S3. The band structure along the high-symmetry paths Γ-X-U | K-Γ-L-W-X and Γ-M-K-Γ-A-L-H-A | L-M | H-K reveals enhanced valence band dispersion along the Γ→L path with band crossing at E_F, while localized conduction bands emerge near the K region. The Fermi level intersects hybridized bands at U | K and forms an energy gap at M. The projected density of states shows broadened Zn 3d states below E_F (−4 to −2 eV) and Cu 3d states near E_F with an unoccupied peak at +0.5 eV, alongside significant Zn/Cu orbital hybridization. These features directly corroborate the Zn→Cu charge transfer mechanism: The enhanced valence band dispersion along Γ-L indicates electron delocalization consistent with Zn electron depletion, while the conduction band localization near K reflects state localization corresponding to Cu electron capture, with the E_F crossing at U | K confirming interfacial charge transfer channels that align with real-space differential charge density observations. EDS was utilized to ascertain the elemental compositions of the $Cu_{0.7}Zn_{0.3}$-ZIF/NF (Figure 2f) and $Cu_{0.5}Zn_{0.5}$-ZIF/NF (Figure S4) catalysts. The corresponding EDS mapping demonstrated that the structures in the nanoflowers were predominantly composed of the elements C, N, and Zn, thereby indicating that the elemental composition of the $Cu_{0.7}Zn_{0.3}$-ZIF/NF was similar to that of ZIF-8. Combined with the coordination of Cu with 2-methylimidazole ligands confirmed by XRD (Figure S1) [43], we propose that it forms a ZIF-like derivative. Additionally, the uniform distribution of Cu elements on the NF surface was found to facilitate the uniform distribution of active sites for the AOR reaction [41]. Furthermore, the EDS data (Figures S5 and S6) demonstrate that the Cu/Zn atomic ratio in $Cu_{0.7}Zn_{0.3}$-ZIF/NF and $Cu_{0.5}Zn_{0.5}$-ZIF/NF approximates the doping ratio, thereby indicating the successful introduction of Cu.

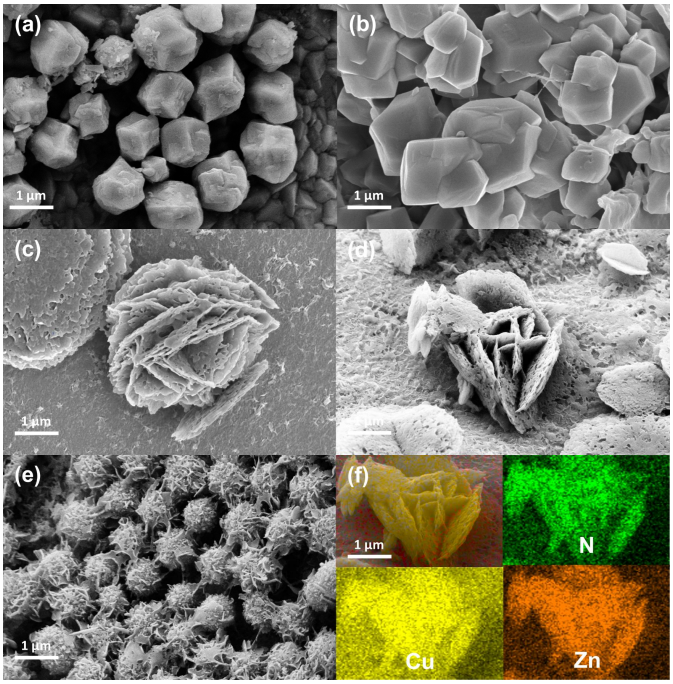


Figure 2. SEM images of (**a**) Zn-ZIF/NF, (**b**) $Cu_{0.3}Zn_{0.7}$-ZIF/NF, (**c**) $Cu_{0.5}Zn_{0.5}$-ZIF/NF, (**d**) $Cu_{0.7}Zn_{0.3}$-ZIF/NF, and (**e**) Cu-ZIF/NF; (**f**) EDS elemental mapping images of $Cu_{0.7}Zn_{0.3}$-ZIF/NF.

In order to further explore the reasons for the changes in the catalyst micromorphology, the Cu_xZn_{1-x}-ZIF/NF series catalysts were examined using X-ray photoelectron spectroscopy (XPS). The XPS results of the catalysts are shown in Figure 3. As illustrated in Figure 3a, the Zn 2p spectra for various catalysts are presented, and the investigation revealed the presence of two primary positions of spectral peaks, with locations in the vicinity of 1021 and 1044 eV, respectively. It has been confirmed that the presence of

Zn^{2+} has been detected [38]. The binding energy at Zn $2p_{1/2}$ shows a gradual increase with elevated Cu doping, from 1021.78 eV for Zn-ZIF/NF to 1021.96 eV for $Cu_{0.7}Zn_{0.3}$-ZIF/NF, which is mainly attributed to the electron density redistribution induced by the high electronegativity of Cu [36]. Cu pulls electrons from the Zn-N ligand environment through metal–ligand bonding, enhancing the effective nuclear charge of Zn. This fine-tuning of the electronic structure optimizes the Lewis acidity of the Zn site, which significantly enhances the ammonia decomposition activity. From the Cu 2p spectrum (Figure 3b), it is evident that all samples exhibited two prominent peaks in the Cu $2p_{1/2}$ region, located at 933 and 934 eV, respectively. These peaks have been identified as Cu^+ and Cu^{2+} species [36,39]. Specifically, the binding energies of the main peaks of the Cu 2p decreased in comparison to those of the Cu-ZIF/NF when the added Cu reached 50% and 70%. This decline was primarily attributable to electron transfer between Cu and Zn, a finding that aligns with the observations made in the Zn 2p spectra. Furthermore, the electron gain of Cu was reflected in its valence change, and the Cu^+ content of $Cu_{0.5}Zn_{0.5}$-ZIF/NF and $Cu_{0.7}Zn_{0.3}$-ZIF/NF was higher than that of Cu-ZIF/NF (56%), reaching 64% and 80%, respectively. The electron transfer between Zn and Cu provided a sufficient active site for the AOR [37]. This results in a significant enhancement of the speed and efficiency of hydrogen production. Consequently, despite the similarity in microstructure exhibited by the $Cu_{0.5}Zn_{0.5}$-ZIF/NF and $Cu_{0.7}Zn_{0.3}$-ZIF/NF catalysts, the latter exhibited a higher content of Cu^+. This result indicates that the higher AOR activity observed in the $Cu_{0.7}Zn_{0.3}$-ZIF/NF catalyst is due to its higher content of Cu^+ (See Figure S7).

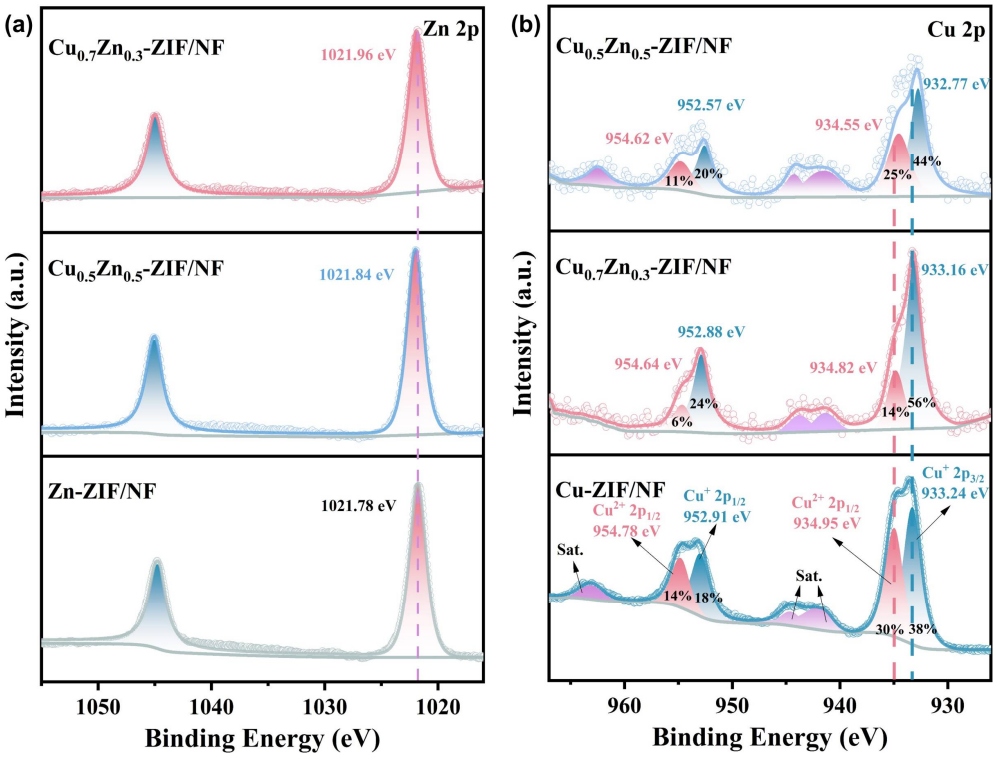


Figure 3. XPS spectra of each Cu_xZn_{1-x}-ZIF/NF catalyst: (**a**) Zn 2p; (**b**) Cu 2p.

3.2. AOR Performance of Catalysts

To evaluate the AOR performance of each catalyst, measurements were conducted on a typical three-electrode system within a 1 M KOH + $NH_3 \cdot H_2O$ electrolyte. The intrinsic activity of the catalysts was tested by LSV. As shown in Figure 4a, the $Cu_{0.7}Zn_{0.3}$-ZIF/NF catalyst had a potential of only 1.4 V (vs. RHE) at a current density of 10 mA/cm^2, representing the lowest potential among all catalysts, highlighting its superior performance.

Furthermore, it delivered an excellent current density of 124 mA/cm^2 at 1.6 V vs. RHE. This enhanced activity is attributed not only to the "nanoflower" microstructure, which provides more exposed active sites and a large interfacial contact area, but also to the contribution of additional Cu sites to AOR performance. In conclusion, the negligible AOR activity of pure NF further confirms that $Cu_{0.7}Zn_{0.3}$-ZIF/NF provides the essential active sites for the reaction.

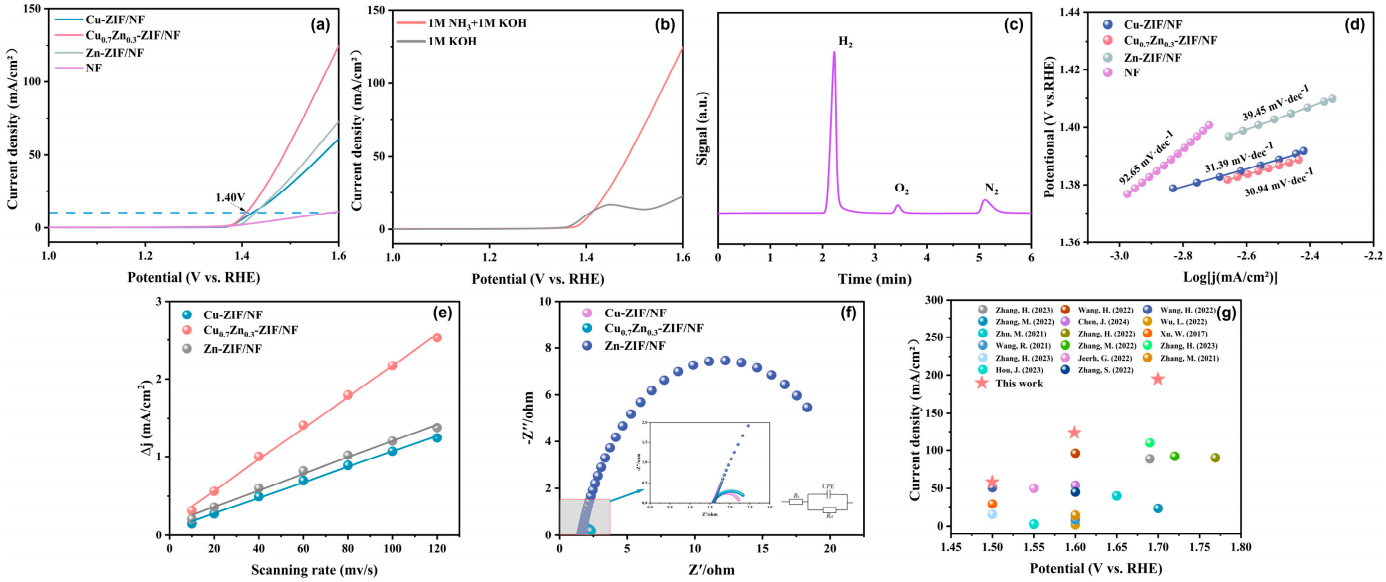


Figure 4. Electrochemical performance tests of Cu_xZn_{1-x}-ZIF/NF in a three-electrode system: (**a**) LSV curves of each catalyst in 1 M KOH + $NH_3 \cdot H_2O$; (**b**) LSV curves of $Cu_{0.7}Zn_{0.3}$-ZIF/NF catalysts in 1 M KOH containing ammonia (without ammonia); (**c**) $Cu_{0.7}Zn_{0.3}$-ZIF/NF catalysts' GC curves; (**d**) Tafel slope of each catalyst; (**e**) C_{dl} of each catalyst; (**f**) EIS comparison of each catalyst; (**g**) AOR performance of $Cu_{0.7}Zn_{0.3}$-ZIF/NF catalysts in comparison with other studies. Comparison [6,11,12,17,18,21,24,39,45–52].

It is well known that the AOR competes with the oxygen evolution reaction (OER) in the process of ammonia electrolysis, and additional tests were performed to confirm that the observer activity primarily stemmed from ammonia oxidation rather than water splitting. A comparison of the LSV curves for the AOR and OER (Figure 4b) reveals significantly higher current densities for the AOR, despite the OER exhibiting a lower onset potential at 10 mA/cm^2. To unequivocally identify the reaction occurring in the 1 M KOH + $NH_3 \cdot H_2O$ electrolyte, gaseous products were analyzed by online GC. The results (Figure 4c) show that the reaction products consist predominantly of H_2 and N_2, with only a minor amount of O_2, confirming that the primary process is an AOR. The Tafel slope analysis (Figure 4d) yielded values of 39.45, 31.39, and 30.94 mV dec^{-1} for Zn-ZIF/NF, Cu-ZIF/NF, and $Cu_{0.7}Zn_{0.3}$-ZIF/NF, respectively. The lower Tafel slope of the $Cu_{0.7}Zn_{0.3}$-ZIF/NF catalyst compared to both Zn-ZIF/ NF and Cu-ZIF/NF indicates superior electrochemical activity, and evidence was found to suggest that an elevated level of Cu^+ is capable of significantly augmenting the catalytic activity of the AOR [37].

To better understand the electrochemical properties, double–double layer capacitance (C_{dl}) and electrochemical ac impedance spectroscopy (EIS) tests were performed (Figure 4e). The C_{dl} values ranked as follows: $Cu_{0.7}Zn_{0.3}$-ZIF/NF (20.09 mF cm^{-2}) > Zn-ZIF/NF (10.58 mF cm^{-2}) > Cu-ZIF/NF (9.94 mF cm^{-2}). $Cu_{0.7}Zn_{0.3}$-ZIF/NF exhibits a higher C_{dl} than the recently reported Ni_1Cu_3@Ni-NDC (12.69 mF cm^{-2}) [39], indicating abundant exposed active sites that facilitate catalyst–reactant contact and further demonstrating its superior performance. This large C_{dl} likely originates from the high BET of the ZIF

material, with Cu doping further enhancing material defect density, leading to an increased electrochemically active surface area (ECSA). Additionally, Cu-doped catalysts (except $Cu_{0.3}Zn_{0.7}$-ZIF/NF, Figure S7) show a higher C_{dl} than Zn-ZIF/NF or Cu-ZIF/NF alone, which suggests a Zn-Cu synergistic effect that enhances catalytic performance.

The EIS results revealed that the complete substitution of Zn by Cu in 2-methylimidazole coordination significantly reduced R_{ct}, which was 0.90 and 0.67 Ω for the $Cu_{0.7}Zn_{0.3}$-ZIF/NF and Cu-ZIF/NF catalysts. The lower R_{ct} of $Cu_{0.7}Zn_{0.3}$-ZIF/NF correlates with its high AOR activity, as reduced R_{ct} facilitates rapid electron transfer, thereby enhancing catalytic reactions and explaining the observed high AOR activity.

In addition to the above tests, stability is a crucial metric for catalytic performance. As shown in Figure S9, the i-t results of $Cu_{0.7}Zn_{0.3}$-ZIF/NF demonstrate excellent stability exceeding 10 h, further confirming its superior catalytic performance. Moreover, to better evaluate this catalyst, we compared it with the recently reported catalysts. Figure 4g shows that it exhibited the highest activity across various potentials, further evidencing its exceptional AOR performance. For a more direct comparison with prior studies, Table 1 summarizes the current density of selected catalysts at specified potentials. The data clearly demonstrate that our catalyst achieves 124 mA/cm^2 at 1.6 V vs. RHE, significantly outperforming other catalysts. Notably, this performance substantially exceeds the 54 mA/cm^2 reported for the recent MOF-based Ni_1Cu_3@Ni-NDC AOR catalyst, further highlighting the superior activity of $Cu_{0.7}Zn_{0.3}$-ZIF/NF. Furthermore, at a higher potential of 1.7 V, it delivers an even higher current density of 195 mA/cm^2, further confirming its exceptional performance under elevated voltage conditions.

Table 1. Comparison of AOR performance with the literature.

Catalyst	Electrolytes	Anode Potential (vs. RHE)	Current Density (mA/cm^2)	Ref.
$Cu_{0.7}Zn_{0.3}$-ZIF/NF	1 M KOH + 1 M NH_3	**1.6 V** **1.7 V**	**124** **195**	**This work**
$Ni_1Cu_1Co_{0.5}$-S-T/CP	1 M NaOH + 0.2 M NH_4Cl	1.6 V	96	Ref. [12]
$NiCu_3$@Ni-NDC	0.5 M KOH + 55 mM NH_3	1.6 V	54	Ref. [39]
LNCO55-Ar	0.5 M KOH + 55 mM NH_4Cl	1.6 V	14	Ref. [6]
Ni_2P/NF	1 M KOH + 5000 mg/L NH_3	1.6 V	8.2	Ref. [18]
α-Fe_2O_3	0.1 M $NaClO_4$ + 0.5 M NH_3	1.6 V	2.13	Ref. [46]
Ni_1Cu_3-S-T/CP	1 M NaOH + 0.2 M NH_4Cl	1.69 V	110	Ref. [24]
Ni_1Cu_3-N-C	1 M NaOH + 0.2 M NH_4Cl	1.69 V	88	Ref. [21]
$Ni_4Cu_5Fe_1$/C	0.5 M KOH + 55 mM NH_3	1.72 V	92	Ref. [52]

4. Conclusions

In this study, the electrocatalytic ammonia decomposition performance was significantly enhanced by the synergistic effect of Cu-doped ZIF-8/NF and structural modifications. The "nanoflower" structure of $Cu_{0.7}Zn_{0.3}$-ZIF/NF increased the exposure of active sites and the reactant transport efficiency, and its high porosity and uniform Cu distribution promoted the AOR kinetics. XPS confirmed the induction of electron transfer between Zn and Cu due to Cu doping, whereby $Cu_{0.7}Zn_{0.3}$-ZIF/NF exhibited the highest Cu^+ content, providing sufficient active sites for the AOR and resulting in excellent catalytic performance. The catalyst achieved a current density of 124 mA/cm^2 at 1.6 V vs. RHE, which was the highest at all potentials when compared with catalysts studied in recent years, and the Tafel slope (30.94 mV dec^{-1}) indicated its efficient charge transfer characteristics. The poor conductivity of MOF materials was solved by the composite strategy of conductive substrate NF and ZIF-8, which provides a new idea for the application of non-noble metal

catalysts in the field of energy conversion. The dynamic valence modulation and bimetallic synergistic mechanism can be further explored in the future.

Supplementary Materials: The following supporting information can be downloaded at https://www.mdpi.com/article/10.3390/en18143871/s1, Figure S1: XRD diffraction patterns of each catalyst; Figure S2: TEM of $Cu_{0.7}Zn_{0.3}$-ZIF/NF; Figure S3: The band structure diagram of (a) Zn and (b) Cu, and (c) differential density of states results for Zn and Cu are presented herewith. In the band structure diagram of zinc, zinc is represented by gray, whereas copper is represented by blue; Figure S4: EDS of $Cu_{0.5}Zn_{0.5}$-ZIF/NF; Figure S5: Elemental atomic content ratio distribution diagram of $Cu_{0.7}Zn_{0.3}$-ZIF/NF catalyst; Figure S6: Elemental atomic content ratio distribution diagram of $Cu_{0.5}Zn_{0.5}$-ZIF/NF catalyst. Figure S7: LSV curves for each ratio of catalysts; Figure S8: C_{dl} performance of each catalyst; Figure S9: Stability testing of $Cu_{0.7}Zn_{0.3}$-ZIF/NF catalysts.

Author Contributions: Methodology, M.O. and G.C.; Investigation, G.C. and W.N.; Data curation, M.O.; Writing—original draft, M.O., G.C. and W.N.; Writing—review & editing, X.W., X.M. and L.M.; Supervision, X.W.; Project administration, L.M.; Funding acquisition, X.W. and L.M. All authors have read and agreed to the published version of the manuscript.

Funding: This work was supported by the Natural Science Foundation of Guangxi Province (Grant No. AB25069268), Basic Ability Promotion Project for Young College Teachers in Guangxi Zhuang Autonomous Region (Grant No. 2025KY0041) and the National Natural Science Foundation of China (Grant No. U21A2054).

Data Availability Statement: The original contributions presented in the study are included in the article/Supplementary Materials, and further inquiries can be directed to the corresponding author.

Conflicts of Interest: The authors declare no conflicts of interest.

References

1. Jilani, A.; Ibrahim, H. Development in photoelectrochemical water splitting using carbon-based materials: A path to sustainable hydrogen production. *Energies* **2025**, *18*, 1603. [CrossRef]
2. Sotiriou, A.; Aspri, E.; Deligiannakis, Y.; Louloudi, M. Engineering of hybrid SiO_2@{N-P-Fe} catalysts with double-ligand for efficient H_2 production from HCOOH. *Energies* **2025**, *18*, 514. [CrossRef]
3. Li, Y.; Li, X.; Pillai, H.S.; Lattimer, J.; Adli, N.M.; Karakalos, S.G.; Chen, M.; Guo, L.; Xu, H.; Yang, J.; et al. Ternary ptirni catalysts for efficient electrochemical ammonia oxidation. *ACS Catal.* **2020**, *10*, 3945–3957. [CrossRef]
4. Mukherjee, S.; Devaguptapu, S.V.; Sviripa, A.; Lund, C.R.; Wu, G. Low-Temperature Ammonia Decomposition Catalysts for Hydrogen Generation. *Appl. Catal. B-Environ.* **2018**, *226*, 162–181. [CrossRef]
5. La Corte, D.; Maddaloni, M.; Vahidzadeh, R.; Domini, M.; Bertanza, G.; Ansari, S.U.; Marchionni, M.; Tola, V.; Artioli, N. Recovered ammonia as a sustainable energy carrier: Innovations in recovery, combustion, and fuel cells. *Energies* **2025**, *18*, 508. [CrossRef]
6. Zhang, M.; Li, H.; Duan, X.; Zou, P.; Jeerh, G.; Sun, B.; Chen, S.; Humphreys, J.; Walker, M.; Xie, K.; et al. An efficient symmetric electrolyzer based on bifunctional perovskite catalyst for ammonia electrolysis. *Adv. Sci.* **2021**, *8*, 2101299. [CrossRef] [PubMed]
7. Adli, N.M.; Zhang, H.; Mukherjee, S.; Wu, G. Review—Ammonia oxidation electrocatalysis for hydrogen generation and fuel cells. *J. Electrochem. Soc.* **2018**, *165*, 3130–3147. [CrossRef]
8. Akagi, N.; Hori, K.; Sugime, H.; Noda, S.; Hanada, N. Systematic investigation of anode catalysts for liquid ammonia electrolysis. *J. Catal.* **2022**, *406*, 222–230. [CrossRef]
9. Zhang, Y.; Wang, J.; Yao, Z. Recent development of fuel cell core components and key materials: A review. *Energies* **2023**, *16*, 2099. [CrossRef]
10. Feng, Y.; Huang, L.; Xiao, Z.; Zhuang, X.; Aslam, T.S.; Zhang, X.; Tan, Y.X.; Wang, Y. Temporally decoupled ammonia splitting by a Zn–NH_3 battery with an ammonia oxidation/hydrogen evolution bifunctional electrocatalyst as a cathode. *J. Am. Chem. Soc.* **2024**, *146*, 7771–7778. [CrossRef] [PubMed]
11. Jeerh, G.; Zou, P.; Zhang, M.; Chen, S.; Humphreys, J.; Tao, S. Electrooxidation of ammonia on a-site deficient perovskite oxide $La_{0.9}Ni_{0.6}Cu_{0.35}Fe_{0.05}O_3$-δ for wastewater treatment. *Sep. Purif. Technol.* **2022**, *297*, 121451. [CrossRef]
12. Wang, H.; Tong, X.; Zhou, L.; Wang, Y.; Liao, L.; Ouyang, S.; Zhang, H. Unique three-dimensional nanoflower-like NiCu electrodes constructed by Co, S co-doping for efficient ammonia oxidation reaction. *Sep. Purif. Technol.* **2022**, *303*, 122293. [CrossRef]

13. Li, Y.; Pillai, H.S.; Wang, T.; Hwang, S.; Zhao, Y.; Qiao, Z.; Mu, Q.; Karakalos, S.; Chen, M.; Yang, J.; et al. High-performance ammonia oxidation catalysts for anion-exchange membrane direct ammonia fuel cells. *Energy Environ. Sci.* **2021**, *14*, 1449–1460. [CrossRef]
14. Shih, Y.-J.; Huang, Y.-H.; Huang, C.P. Electrocatalytic ammonia oxidation over a nickel foam electrode: Role of $Ni(OH)_{2(s)}$-$NiOH_{(s)}$ nanocatalysts. *Electrochim. Acta* **2018**, *263*, 261–271. [CrossRef]
15. Kim, H.; Yang, W.; Lee, W.H.; Han, M.H.; Moon, J.; Jeon, C.; Kim, D.; Ji, S.G.; Chae, K.H.; Lee, K.-S.; et al. Operando stability of platinum electrocatalysts in ammonia oxidation reactions. *ACS Catal.* **2020**, *10*, 11674–11684. [CrossRef]
16. Siddharth, K.; Hong, Y.; Qin, X.; Lee, H.J.; Chan, Y.T.; Zhu, S.; Chen, G.; Choi, S.-I.; Shao, M. Surface engineering in improving activity of pt nanocubes for ammonia electrooxidation reaction. *Appl. Catal. B-Environ.* **2020**, *269*, 118821. [CrossRef]
17. Zhu, M.; Yang, Y.; Xi, S.; Diao, C.; Yu, Z.; Lee, W.S.V.; Xue, J. Deciphering NH_3 adsorption kinetics in ternary Ni–Cu–Fe oxyhydroxide toward efficient ammonia oxidation reaction. *Small* **2021**, *17*, 2005616. [CrossRef] [PubMed]
18. Wang, R.; Liu, H.; Zhang, K.; Zhang, G.; Lan, H.; Qu, J. Ni(ii)/Ni(iii) redox couple endows Ni foam-supported Ni_2P with excellent capability for direct ammonia oxidation. *Chem. Eng. J.* **2021**, *404*, 126795. [CrossRef]
19. Xue, Q.; Zhao, Y.; Zhu, J.; Ding, Y.; Wang, T.; Sun, H.; Li, F.; Chen, P.; Jin, P.; Yin, S.; et al. Ptru nanocubes as bifunctional electrocatalysts for ammonia electrolysis. *J. Mater. Chem. A* **2021**, *9*, 8444–8451. [CrossRef]
20. Moran, E.; Cattaneo, C.; Mishima, H.; de Mishima, B.A.L.; Silvetti, S.P.; Rodriguez, J.L.; Pastor, E. Ammonia oxidation on electrodeposited Pt–Ir alloys. *J. Solid. State Electrochem.* **2007**, *12*, 583–589. [CrossRef]
21. Zhang, H.; Wang, H.; Zhou, L.; Li, Q.; Yang, X.; Wang, Y.; Zhang, M.; Wu, Z. Efficient and highly selective direct electrochemical oxidation of ammonia to dinitrogen facilitated by nicu diatomic site catalysts. *Appl. Catal. B-Environ.* **2023**, *328*, 122544. [CrossRef]
22. Zhang, S.; Jiang, H.; Yan, L.; Zhao, Y.; Yang, L.; Fu, Q.; Li, D.; Zhang, J.; Zhao, X. Self-terminating surface reconstruction induced by high-index facets of delafossite for accelerating ammonia oxidation reaction involving lattice oxygen. *Small* **2023**, *19*, e2207727. [CrossRef] [PubMed]
23. Jo, C.; Surendran, S.; Kim, M.-C.; An, T.-Y.; Lim, Y.; Choi, H.; Janani, G.; Jesudass, S.C.; Moon, D.J.; Kim, J.; et al. Meticulous integration of n and c active sites in Ni_2P electrocatalyst for sustainable ammonia oxidation and efficient hydrogen production. *Chem. Eng. J.* **2023**, *463*, 142314. [CrossRef]
24. Zhang, H.; Wang, H.; Tong, X.; Zhou, L.; Yang, X.; Wang, Y.; Zhang, M.; Wu, Z. Sulfur induced surface reconfiguration of $Ni1Cu_3$-S-T/CP anode for high-efficiency ammonia electro-oxidation. *Chem. Eng. J.* **2023**, *452*, 139582. [CrossRef]
25. Chai, L.; Pan, J.; Hu, Y.; Qian, J.; Hong, M. Rational design and growth of MOF-on-MOF heterostructures. *Small* **2021**, *17*, 2100607. [CrossRef] [PubMed]
26. Yang, S.; Peng, L.; Syzgantseva, O.A.; Trukhina, O.; Kochetygov, I.V.; Justin, A.; Sun, D.T.; Abedini, H.; Syzgantseva, M.A.; Oveisi, E.; et al. Preparation of highly porous metal—organic framework beads for metal extraction from liquid streams. *J. Am. Chem. Soc.* **2020**, *142*, 13415–13425. [CrossRef] [PubMed]
27. Chen, M.; Liu, T.; Zhang, X.; Zhang, R.; Tang, S.; Yuan, Y.; Xie, Z.; Liu, Y.; Wang, H.; Fedorovich, K.V.; et al. Photoinduced enhancement of uranium extraction from seawater by MOF/black phosphorus quantum dots heterojunction anchored on cellulose nanofiber aerogel. *Adv. Funct. Mater.* **2021**, *31*, 2100106. [CrossRef]
28. Bai, Y.; Liu, C.; Chen, T.; Li, W.; Zheng, S.; Pi, Y.; Luo, Y.; Pang, H. Mxene-Copper/Cobalt hybrids via lewis acidic molten salts etching for high performance symmetric supercapacitors. *Angew. Chem.-Int. Edit.* **2021**, *60*, 25318–25322. [CrossRef] [PubMed]
29. Chen, T.; Wang, F.; Cao, S.; Bai, Y.; Zheng, S.; Li, W.; Zhang, S.; Hu, S.; Pang, H. In situ synthesis of MOF-74 family for high areal energy density of aqueous Nickel–Zinc batteries. *Adv. Mater.* **2022**, *34*, e2201779. [CrossRef] [PubMed]
30. Du, M.; Geng, P.; Pei, C.; Jiang, X.; Shan, Y.; Hu, W.; Ni, L.; Pang, H. High-entropy prussian blue analogues and their oxide family as sulfur hosts for lithium-sulfur batteries. *Angew. Chem.-Int. Edit.* **2022**, *61*, e202209350. [CrossRef] [PubMed]
31. Fan, L.; Guo, X.; Hang, X.; Pang, H. Synthesis of truncated octahedral zinc-doped manganese hexacyanoferrates and low-temperature calcination activation for lithium-ion battery. *J. Colloid. Interface Sci.* **2022**, *607*, 1898–1907. [CrossRef] [PubMed]
32. Geng, P.; Du, M.; Wu, C.; Luo, T.; Zhang, Y.; Pang, H. Ppy-constructed core–shell structures from MOFs for confining lithium polysulfides. *Inorg. Chem. Front.* **2022**, *9*, 2389–2394. [CrossRef]
33. Guo, X.; Li, W.; Geng, P.; Zhang, Q.; Pang, H.; Xu, Q. Construction of SiO/nitrogen-doped carbon superstructures derived from rice husks for boosted lithium storage. *J. Colloid. Interface Sci.* **2022**, *606*, 784–792. [CrossRef] [PubMed]
34. Al-Janabi, N.; Hill, P.; Torrente-Murciano, L.; Garforth, A.; Gorgojo, P.; Siperstein, F.; Fan, X. Mapping the Cu-btc metal—organic framework (HKUST-1) stability envelope in the presence of water vapour for CO_2 adsorption from flue gases. *Chem. Eng. J.* **2015**, *281*, 669–677. [CrossRef]
35. Migunova, A.A.; Nemkayeva, R.R.; Zhakanbayev, Y.A.; Tuleushev, Y.Z. One-step synthesis $CuCoNiS_xO_{4-x}$ thio/oxy spinel on Ni foam for high-performance asymmetric supercapacitors. *Energies* **2025**, *18*, 561. [CrossRef]
36. Song, X.; Han, B.; Yu, X.; Hu, W. The analysis of charge transport mechanism in molecular junctions based on current-voltage characteristics. *Chem. Phys.* **2020**, *528*, 110514. [CrossRef]

37. Liu, Y.; Cai, Y.; Yang, Z.; Shen, Y.; Wang, X.; Song, X.; Mu, X.; Gao, J.; Zhou, J.; Miao, L. High-performance NiCu hydroxide self-supported electrode as a bifunctional catalyst for AOR and OER. *Battery Energy* **2025**, *4*, e70010. [CrossRef]
38. Ma, Z.Q.; Han, C.B.; Zhao, W.K.; Fang, D.C.; Zhao, Y.L.; Liu, C.X.; Wang, X.; Sun, L.; Song, X.M. Formaldehyde oxidation reaction enhanced by interface engineering of $Cu/Cu_2O/Co(OH)_2$ composite electrocatalyst for bipolar hydrogen production. *Chem. Eng. J.* **2025**, *512*, 162568. [CrossRef]
39. Chen, J.; Chen, H.; Wang, Z.; Fu, Y.; Yu, D.; Liang, J.; Huang, Y.; Wang, L.; Bello, I.T.; Ekambo, G.N.; et al. Cu-improving ammonia oxidation to nitrogen across wide potential range via synergistic effect over Cu and Ni anchored metal-organic frameworks. *Chem. Eng. J.* **2024**, *499*, 156283. [CrossRef]
40. Huang, J.; Cai, J.; Wang, J. Cu-nanostructured wire-in-plate electrocatalyst for high-durability production of hydrogen and nitrogen from alkaline ammonia solution. *ACS Appl. Energ. Mater.* **2020**, *3*, 4108–4113. [CrossRef]
41. Vu, H.K.; Mahvelati-Shamsabadi, T.; Dang, T.T.; Hur, S.H.; Kang, S.G.; Chung, J.S. Cu-synergistic effects of Ni and Cu in morphology-controlled NiCu electrocatalysts for ammonia electro-oxidation. *ACS Appl. Nano Mater.* **2023**, *6*, 20688–20699. [CrossRef]
42. Xu, W.; Du, D.; Lan, R.; Humphreys, J.; Miller, D.N.; Walker, M.; Wu, Z.; Irvine, J.T.; Tao, S. Cu-electrodeposited NiCu bimetal on carbon paper as stable non-noble anode for efficient electrooxidation of ammonia. *Appl. Catal. B-Environ.* **2018**, *237*, 1101–1109. [CrossRef]
43. Lee, K.; Vikneshvaran, S.; Lee, H.; Lee, S.-Y. Ligand-mediated electrocatalytic activity of Cu-imidazolate coordination polymers for OER in water electrolysis. *Int. J. Hydrogen Energy* **2024**, *51*, 1184–1196. [CrossRef]
44. Velisoju, V.K.; Cerrillo, J.L.; Ahmad, R.; Mohamed, H.O.; Attada, Y.; Cheng, Q.; Yao, X.; Zheng, L.; Shekhah, O.; Telalovic, S.; et al. Copper nanoparticles encapsulated in zeolitic imidazolate framework-8 as a stable and selective CO_2 hydrogenation catalyst. *Nat. Commun.* **2024**, *15*, 2045. [CrossRef] [PubMed]
45. Hou, J.; Cheng, Y.; Pan, H.; Kang, P. Tailored bimetallic Ni–Sn catalyst for electrochemical ammonia oxidation to dinitrogen with high selectivity. *Inorg. Chem.* **2023**, *62*, 3986–3992. [CrossRef] [PubMed]
46. Wu, L.; Tang, D.; Xue, J.; Liu, S.; Wang, J.; Ji, H.; Chen, C.; Zhang, Y.; Zhao, J. Competitive non-radical nucleophilic attack pathways for NH_3 oxidation and H_2O oxidation on hematite photoanodes. *Angew. Chem.-Int. Edit.* **2022**, *61*, e202214580. [CrossRef] [PubMed]
47. Zhang, H.; Chen, W.; Wang, H.; Tong, X.; Wang, Y.; Yang, X.; Wu, Z.; Liu, Z. A core-shell NiCu@NiCuOOH 3D electrode induced by surface electrochemical reconstruction for the ammonia oxidation reaction. *Int. J. Hydrogen Energy* **2022**, *47*, 16080–16091. [CrossRef]
48. Zhang, H.; Tong, X.; Wang, H.; Zhou, L.; Huang, S.; Li, D.; Wang, Y.; Xiao, H.; Zhang, M. Efficient ammonia removal promoted in a bifunctional system constructed with NiCu–S/DSA electrodes. *J. Clean. Prod.* **2023**, *415*, 137636. [CrossRef]
49. Zhang, M.; Zou, P.; Jeerh, G.; Sun, B.; Walker, M.; Tao, S. Oxygen vacancy-rich $La_{0.5}Sr_{1.5}Ni_{0.9}Cu_{0.1}O_4$–δ as a high-performance bifunctional catalyst for symmetric ammonia electrolyzer. *Adv. Funct. Mater.* **2022**, *32*, 2204881. [CrossRef]
50. Zhang, S.; Yan, L.; Jiang, H.; Yang, L.; Zhao, Y.; Yang, X.; Wang, Y.; Shen, J.; Zhao, X. Facile fabrication of a foamed Ag_3CuS_2 film as an efficient self-supporting electrocatalyst for ammonia electrolysis producing hydrogen. *ACS Appl. Mater. Interfaces* **2022**, *14*, 9036–9045. [CrossRef] [PubMed]
51. Xu, W.; Lan, R.; Du, D.; Humphreys, J.; Walker, M.; Wu, Z.; Wang, H.; Tao, S. Directly growing hierarchical nickel-copper hydroxide nanowires on carbon fibre cloth for efficient electrooxidation of ammonia. *Appl. Catal. B-Environ.* **2017**, *218*, 470–479. [CrossRef]
52. Zhang, M.; Zhang, J.; Jeerh, G.; Zou, P.; Sun, B.; Walker, M.; Xie, K.; Tao, S. A symmetric direct ammonia fuel cell using ternary NiCuFe alloy embedded in a carbon network as electrodes. *J. Mater. Chem. A* **2022**, *10*, 18701–18713. [CrossRef]

Disclaimer/Publisher's Note: The statements, opinions and data contained in all publications are solely those of the individual author(s) and contributor(s) and not of MDPI and/or the editor(s). MDPI and/or the editor(s) disclaim responsibility for any injury to people or property resulting from any ideas, methods, instructions or products referred to in the content.